Chemical Science

ROYAL SOCIETY OF CHEMISTRY

EDGE ARTICLE

View Article Online
View Journal

Cite this: DOI: 10.1039/d5sc03817k

All publication charges for this article have been paid for by the Royal Society of Chemistry

Molecular design of sensitizers for high-efficiency OLEDs: exploration of energy transfer dynamics

Xiao Liu,†[a] Xue-liang Wen,†[b] Yang Zhou,[a] Chao Tang,[a] Diandong Tang,[c] Qian Wang,[a] Yibo Shi,[a] Lin Liu,[a] Wei Sun,[a] Kai Feng,[a] Wei-Hai Fang,*[a] Juan Qiao,*[b] Lin Shen*[a] and Xuebo Chen*[ad]

As a class of functional materials used in organic light-emitting diodes (OLEDs), sensitizers play a crucial role in the improvement of device efficiency, color purity, and stability. In recent years, thermally activated delayed fluorescence (TADF) sensitizers have attracted much attention mainly because of their high exciton utilization efficiency by converting quenched triplet excitons into singlet excitons. Despite the experimental success of sensitization strategies in enhancing OLED performance, the lack of theoretical models for sensitizers continues to hinder further development. In the present work, we design three novel sensitizers and investigate their photophysical mechanisms in the presence of a host and/or an emitter. Based on highly accurate electronic structure calculations and non-radiative transition rates, we propose the first theoretical model to describe the dynamic behavior of sensitizers in OLEDs. This model highlights key factors for achieving ultraefficient sensitization, such as multi-channel energy transfer capabilities, large intermolecular electronic couplings, and reduced redundant energy transfer pathways in devices as well as conformational rigidity under excitation and small singlet–triplet energy splitting for ideal sensitizers. In particular, a binary system consisting of a new sensitizer as the host material and an emitter achieves excellent performance with a high external quantum efficiency of 29.2% and negligible efficiency roll-off of 5.5% at a brightness of 1000 cd m^{-2} for red phosphorescent OLEDs. These findings provide fundamental chemical insights into exciton dynamics and practical guidelines for material-device co-optimization in next-generation electroluminescent technologies.

Received 26th May 2025
Accepted 12th August 2025

DOI: 10.1039/d5sc03817k

rsc.li/chemical-science

Introduction

Organic light-emitting diodes (OLEDs) are regarded as the cornerstone of next-generation information display technology because of their exceptional characteristics such as self-emission, wide viewing angles, high display quality, rapid response, and flexibility.[1–3] The luminescence mechanism of OLEDs is based on carrier injection and recombination to form excitons, and their luminescence efficiency and stability highly depend on the utilization efficiency of excitons in singlet and triplet states.[4,5] Sensitizers, a class of functional materials used in OLEDs, are able to enhance exciton utilization efficiency *via* an "energy relay network", in which the exciton energy is transferred from the host material or the sensitizer itself to the terminal emitter, thereby improving device efficiency, color purity, and stability.[6–8] Sensitizers can be categorized into two types, *i.e.*, phosphorescent sensitizers and thermally activated delayed fluorescence (TADF) sensitizers. The former type such as iridium (Ir) and platinum complexes exhibits a strong spin–orbit coupling (SOC) effect and captures both singlet and triplet excitons to achieve 100% exciton utilization. However, its application is still limited by the reliance on noble metals and poor stability in blue-light applications.[3,7,9,10] TADF sensitizers, on the other hand, can efficiently convert otherwise quenched triplet excitons into singlet excitons through a fast reverse intersystem crossing (RISC) process at the microsecond timescale.[11–14] In particular, through-space charge transfer (TSCT)-based TADF materials have attracted considerable attention due to their exceptional molecular design versatility. By precisely modulating the spatial separation, orientation, and electronic configuration of donor (D)–acceptor (A) units, these materials can optimize the ΔE_{ST} energy gap and accelerate RISC processes.[15–17] This approach not only exceeds the 25% internal quantum efficiency limit of traditional fluorescent

[a]*Key Laboratory of Theoretical and Computational Photochemistry of the Chinese Ministry of Education, College of Chemistry, Beijing Normal University, Beijing 100875, P. R. China. E-mail: fangwh@bnu.edu.cn; lshen@bnu.edu.cn; xuebochen@bnu.edu.cn*

[b]*Key Lab of Organic Optoelectronics and Molecular Engineering of Ministry of Education, Department of Chemistry, Tsinghua University, Beijing, 100084, P. R. China. E-mail: qjuan@mail.tsinghua.edu.cn*

[c]*Department of Chemistry, University of Washington, Seattle, Washington 98195, USA*

[d]*College of Chemistry and Molecular Sciences, Henan University, Zhengzhou 450046, P. R. China. E-mail: xuebochen@bnu.edu.cn*

† These authors contributed equally (Xiao Liu and Xue-liang Wen).

materials,[18–21] but also circumvents the reliance on noble metals in phosphorescent materials.[22–25]

In devices, energy transfer (EnT), a process *via* which exciton energy is transferred from a donor (*e.g.*, a host material or sensitizer) to an acceptor (*e.g.*, an emitter), is a key factor in the luminescence efficiency, spectral stability and efficiency roll-off. Förster resonance EnT (FRET) relies on dipole–dipole interactions between the donor and acceptor at nanometer distances, while triplet–triplet EnT (TTET, also named Dexter EnT) involves electron exchange *via* molecular orbital overlap between the donor and acceptor at a much shorter distance.[26,27] Different energy transfer mechanisms have been proposed recently. For example, Lee *et al.* observed that phosphorescent sensitizers with higher dipole orientation exhibited a faster rate for direct energy transfer from the triplet to singlet states, resulting in a 2.2-fold increase in the triplet consumption rate of phosphorescent sensitizers.[28] Bronstein and co-workers developed an ultra-narrowband blue emitter encapsulated by bulky alkyl chains, demonstrating that the encapsulation material can suppress the TTET channel from the sensitizer to the terminal emitter. This effect is beneficial to form fluorescent emitters *via* the FRET channel, thereby enhancing device efficiency.[29] Based on the multiple sensitization processes relevant to FRET, Duan and co-workers designed a device using a newly developed indolocarbazole/triazine derivative as the host and achieved a maximum external quantum efficiency (EQE_{max}) of 23.2% and a power efficiency (PE) of 76.9 lm per W.[8]

Despite the experimental success of sensitization strategies in enhancing OLED performance, the lack of theoretical models for sensitizers continues to hinder further development. However, for a typical host–guest system in the presence of an additional sensitizer, the competition between FRET and TTET, the coupling between EnT and TADF, and the relationship between transition rates and molecular structures are still unclear, mainly limited by the accuracy of computational tools. Our group has developed a computational protocol by combining the complete active space self-consistent field method and its second-order perturbation theory (CASSCF//CASPT2) with the non-radiative transition rate models based on Fermi's golden rule.[30–34] In the past decade, it has been

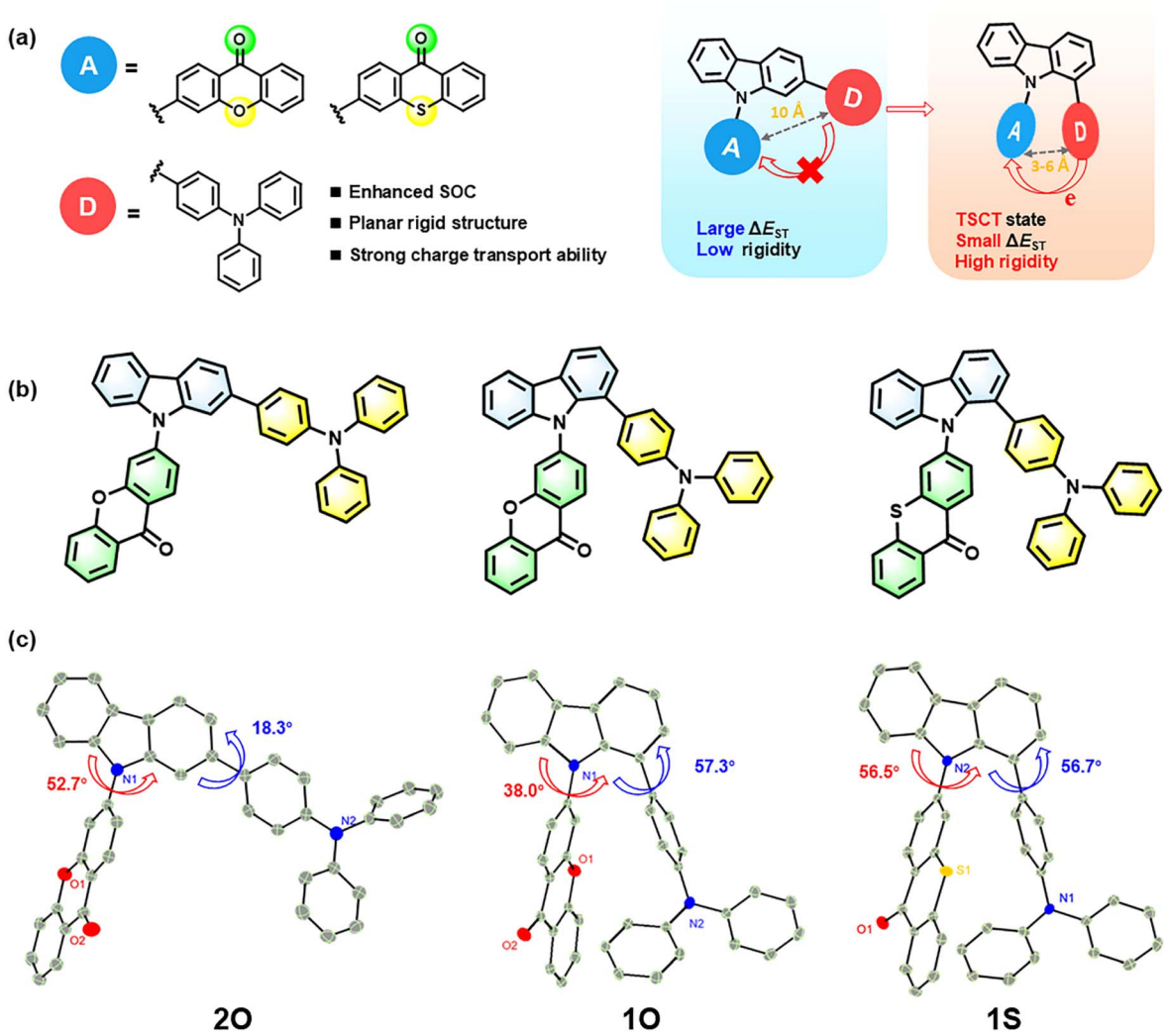

Fig. 1 Molecular design strategy (a) and molecular structures (b) for 2O, 1O and 1S. (c) ORTEP diagrams of 2O, 1O and 1S with thermal ellipsoids drawn at 50% probability. Solvent and hydrogen atoms are omitted.

successfully used to establish a quantitative relationship between intermolecular distances and EnT rates in white OLEDs and to explore the underlying mechanisms of several photocatalytic reactions.[35–37]

In this study, we extend the protocol to build the first theoretical model at the *ab initio* computational level for sensitizers in binary and ternary systems. Guided by a precision molecular orbital engineering strategy, we innovatively introduced carbonyl and sulfur atoms into donor–acceptor (D–A)-type TADF sensitizers. Specifically, the heavy atom effect of sulfur significantly enhances the SOC strength. By employing planar rigid frameworks—xanthone (XT) and thioxanthone (TX) as electron acceptors and precisely modulating the spatial separation between the triphenylamine (TPA) donor and acceptors through a carbazole (Cz) bridging unit, we effectively suppress exciton quenching induced by π–π stacking. Simultaneously, the strong electron-donating capability and three-dimensional stereoscopic configuration of TPA optimize carrier injection efficiency while regulating excited-state energy levels (Fig. 1a). Through atomic-scale tuning of donor–acceptor distances, three novel sensitizers were successfully designed and synthesized: 3-(2-(4-(diphenylamino)phenyl)-9*H*-carbazol-9-yl)-9*H*-xanthen-9-one (**2O**), 3-(1-(4-(diphenylamino)phenyl)-9*H*-carbazol-9-yl)-9*H*-xanthen-9-one (**1O**), and 3-(1-(4-(diphenylamino)phenyl)-9*H*-carbazol-9-yl)-9*H*-thioxanthen-9-one (**1S**). Subsequently, in device architecture construction, we implemented a theory-experiment co-design strategy by integrating tris(4-carbazoyl-9-ylphenyl) amine (TCTA) as the host and bis[2-(1-isoquinolinyl-κN)-4,6-dimethylphenyl-κC](2,4-pentanedionato-κO2,κO4)iridium ($Ir(mpiq)_2acac$, denoted as the Ir(III) complex hereafter) as the terminal emitter and the synthesized sensitizers. Through computational simulations of the excited-state electronic structures and associated energy transfer dynamics, we elucidated the energy transfer mechanisms between sensitizers and host–guest materials, thereby systematically establishing key design principles for high-efficiency OLED sensitizers.

Methods

Computational methods

Electronic structure calculations were performed for TCTA, the Ir(III) complex and the three sensitizer molecules. The ground-state (S_0) and the first triplet-state (T_1) structures at minima were initially optimized at the density functional theory (DFT) level using the B3LYP functional,[38–40] followed by frequency analysis for transition rate calculations. These structures were further optimized at the complete active space self-consistent field (CASSCF) level.[41] The structures in the excited singlet states were optimized using a state-averaged CASSCF calculation. To account for dynamic correlation effects, all single-point energies with key structures were recalculated at the multi-configurational second-order perturbation theory (CASPT2) level.[42–44] The vertical excitation energies with oscillator strengths (*f*) and the spin–orbit coupling constants between the singlet and triplet states were calculated with the multi-root state-averaged CASSCF state interaction (CASSI) method. More details of basis set selection, orbital localization and configuration optimization can be seen in Section S8 (see the SI). All electronic structure calculations were performed using Molcas 8.0 (ref. 45) and Gaussian 16 (ref. 46) software packages.

Based on the above electronic structure calculations, the intermolecular energy transfer rates can be estimated using the method within the general formalism of non-radiative transition models, which was first developed by Lin *et al.*[30–34] and has been successfully applied to explore the mechanisms of white OLEDs and photocatalytic reactions by our group.[35–37,47,48] Starting from the Born–Oppenheimer approximation and Fermi's golden rule, the energy transfer rate constant is given by

$$W_{i\to f} = \frac{2\pi}{\hbar}\cdot\left|\left\langle \Phi_i\middle|\hat{H}'\middle|\Phi_f\right\rangle\right|^2\cdot\sum_{u,v}P_{iu}\left|\langle\Theta_{iu}|\Theta_{fv}\rangle\right|^2\delta\left(E_{fv}-E_{iu}\right) \quad (1)$$

where Φ and Θ represent electronic and vibrational wavefunctions, respectively, i and f denote the initial and final adiabatic electronic states, respectively, u and v denote nuclear vibrational states corresponding to electronic states i and f, respectively, $\hat{H}'$ is the nonadiabatic transition operator to perturb the system from state i to f, E_{iu} and E_{fv} are energies of vibronic states, and P_{iu} is the Boltzmann factor.

The nuclear part in eqn (1), which is the so-called Franck–Condon (FC) term, can be calculated based on the multidimensional harmonic oscillator model as

$$\sum_{u,v}P_{iu}\left|\langle\Theta_{iu}|\Theta_{fv}\rangle\right|^2\delta\left(E_{fv}-E_{iu}\right)=\frac{1}{2\pi\hbar}\int \mathrm{d}t\ \mathrm{e}^{\mathrm{i}t\omega_{i\to f}}\prod_j G_j(t) \quad (2)$$

where

$$G_j(t)=\sum_{u_j,v_j}P_{iu_j}\left|\left\langle\chi_{iu_j}\middle|\chi_{fv_j}\right\rangle\right|^2\mathrm{e}^{\mathrm{i}t\left(v_j+\frac{1}{2}\right)\omega_j}\ \mathrm{e}^{-\mathrm{i}t\left(u_j+\frac{1}{2}\right)\omega_j} \quad (3)$$

Here, χ denotes the nuclear wavefunction of harmonic oscillators, ω_j is the vibrational frequency of the jth normal mode, and $\omega_{i\to f}$ is the adiabatic energy difference between electronic states i and f. Numerical implementations of eqn (2) and (3) can be seen in our previous studies.[35,36]

For the TTET process, the electronic part in eqn (1) can be represented as the square of electronic coupling between two electronic states of the donor–acceptor complex, that is,

$$\left|\left\langle \Phi_i\middle|\hat{H}'\middle|\Phi_f\right\rangle\right|^2_{TTET}=\left\langle\varphi_{D^*}(1)\varphi_A(2)\middle|\frac{1}{r_{12}}\middle|\varphi_{A^*}(1)\varphi_D(2)\right\rangle^2$$
$$=\sum_{i,j,k,l}c_i(\varphi_{D^*})c_j(\varphi_{A^*})c_k(\varphi_A)c_l(\varphi_D)(ij|kl) \quad (4)$$

where φ_{D^*}, φ_D, φ_{A^*} and φ_A are singly occupied orbitals of the donor (D) and acceptor (A), respectively, 1 and 2 denote the two exchanged electrons during TTET, $(ij|kl)$ denotes a two-electron integral with (i, j) and (k, l) as the basis sets associated with electrons 1 and 2, respectively, and c is the coefficient of the singly occupied orbitals.

For the FRET process, the electronic part in eqn (1) is often approximated as classical dipole–dipole interactions between the donor and acceptor.[49,50] However, it is unrealistic in OLED

devices developed in this work. For an emission layer doped at a concentration of 5 wt%, there is always a guest molecule in close proximity to a host molecule at a distance of less than 1 nm, possibly generating a donor–acceptor complex. Therefore, we calculate the electronic part under TTET and FRET on the same footing. In the latter case, eqn (4) can be rewritten as

$$\left|\left\langle \Phi_i \middle| \hat{H}' \middle| \Phi_f \right\rangle\right|^2_{\mathrm{FRET}} = \left\langle \varphi_{D^*}(1)\varphi_A(2)\left|\frac{1}{r_{12}}\right|\varphi_D(1)\varphi_{A^*}(2)\right\rangle^2 = \sum_{i,j,k,l} c_i(\varphi_{D^*})c_j(\varphi_D)c_k(\varphi_A)c_l(\varphi_{A^*})(ij|kl) \quad (5)$$

The notations in eqn (5) are the same as those in eqn (4). Unlike the nuclear part that requires electronic structure calculations on the isolated donor and isolated acceptor in different electronic states, the ground-state calculation of the donor–acceptor complex is necessary to deal with eqn (4) and (5).

Synthesis and characterization

Using 1-bromocarbazole, 4-boronophenylamine, 2-bromooxanthone, 2-bromothioxanthone, and 2-bromoselenoxanthone as substrates, three compounds, **2O**, **1O**, and **1S** (Fig. 1b), were successfully synthesized *via* Suzuki coupling and Buchwald–Hartwig coupling reactions, achieving good yields (>60%) (see Scheme S1 in the SI). All intermediates were purified through column chromatography, and the final products were further purified by column chromatography and recrystallization. Comprehensive characterization data for all compounds, including ^{1}H NMR, ^{13}C NMR, HRMS (high-resolution mass spectrometry), and single-crystal X-ray diffraction (XRD) analysis, were obtained. The single crystals of **2O**, **1O**, and **1S** were grown by slow diffusion in an ethanol/dichloromethane (V/V = 3 : 1) mixed solution, as detailed in Fig. 1c and Tables S1–S3 (see SI). As shown in Fig. 1c, single-crystal structure analysis reveals that all compounds exhibit significantly distorted spatial configurations. Specifically, the dihedral angles between XT/TX acceptor units and adjacent carbazole bridges are 52.7° (**2O**), 38.0° (**1O**), and 56.5° (**1S**), respectively, while the dihedral angles between the TPA donor units and carbazole bridges are 18.3° (**2O**), 57.3° (**1O**), and 56.7° (**1S**), respectively. Notably, compounds **1O** and **1S** demonstrate greater structural distortion (dihedral angles >50°), which effectively suppresses intermolecular π–π stacking interactions. Further analysis shows that the minimum donor–acceptor (D–A) distances in **1O** and **1S** are approximately 5.5 Å, falling within the optimal range for TSCT interactions (typically 3–6 Å)[53–55] and thus facilitating efficient thermally activated delayed fluorescence. In contrast, the D–A distance in **2O** reaches 10 Å, significantly exceeding the effective range for TSCT, which may prevent **2O** from exhibiting TADF characteristics.

Results and discussion

Photophysical properties of sensitizers

The photophysical properties of **2O**, **1O**, and **1S** were investigated in dilute toluene solutions (10^{-5} M) and in thin-film states. The results are shown in Fig. 2 and summarized in Table 1. The significant absorption peaks observed between 280 and 330 nm are attributed to localized π–π* transitions, while a weaker absorption peak in the range of 330–380 nm is ascribed to intramolecular TSCT from the TPA group to the TX or XT acceptors. The S_1 and T_1 energy levels were estimated based on the fluorescence and phosphorescence emission spectra measured at 77 K. We determined the singlet–triplet energy gaps (ΔE_{ST}) for **2O**, **1O**, and **1S** in toluene solution to be 0.66, 0.07, and 0.00 eV, respectively, which are consistent with the theoretically calculated values of 0.72, −0.04, and 0.05 eV (see Fig. 2a–c and Table S8 in the SI). Furthermore, the photoluminescence spectra of these compounds were measured in various solvents (see Fig. S2d–f in the SI). Notably, two emission bands were observed, labeled as F1 and F2, corresponding to short-wavelength and long-wavelength emissions, respectively. The F1 emission band is insensitive to solvent changes, with no significant shift in emission wavelength as solvent polarity varies, indicating a localized excitation (LE) emission. In contrast, the F2 emission spectra exhibit a red shift in polar solvents, which suggests that these compounds possess ICT characteristics. The photoluminescence decay curves in the four solvents all show nanosecond-scale lifetimes (Fig. S2a–c in the SI).

Further measurements of the fluorescence and phosphorescence spectra of their neat thin films at 77 K were conducted (Fig. 2d–f). By analyzing the fluorescence and phosphorescence in the neat films, the values of ΔE_{ST} were estimated to be 0.37, 0.11, and 0.09 eV for **2O**, **1O**, and **1S**, respectively. The relatively small ΔE_{ST} values of **1O** and **1S** suggest their potential for TADF characteristics. In contrast, the larger ΔE_{ST} of **2O** may hinder the occurrence of the TADF process. The same tendency was observed in doped thin films (30 wt% in TCTA). To confirm their TADF properties, we measured transient photoluminescence decay curves of **1O** and **1S** in neat and doped thin films at 298 K. As shown in Fig. 2e, f, S4c and d, typical TADF behavior appears with both prompt (τ_p) and delayed (τ_d) lifetime components. The values of τ_p for **1O** and **1S** in neat/doped thin films are 162.8/135.6 and 76.8/63.6 ns, respectively, and the corresponding τ_d values are 14.23/17.12 μs for **1O** and 3.56/7.07 μs for **1S**. In contrast, the decay curve of **2O** overlaps with the instrument response function and shows a single-exponential decay, indicating that **2O** does not exhibit delayed fluorescence in either neat or doped films (Fig. 2i and S4). Furthermore, the transition rate constants for intersystem crossing (k_{ISC}), reverse intersystem crossing (k_{RISC}), radiative transition ($k_{r,s}$), and non-radiative transition ($k_{nr,s}$) can be obtained from experimental measurements using a previously reported model[51] (Table S4). As expected, the heavy atom effect of sulfur and the small ΔE_{ST} of **1S** lead to faster ISC and RISC rates in its doped film, which are an order of magnitude higher than those of **1O**. The values of k_{RISC} for **1O** in neat and doped thin films are 1.29×10^5 and 0.98×10^5 s^{-1}, respectively, and those for **1S** are 1.21×10^6 and 0.84×10^6 s^{-1} (Table 1). Compared to other luminescent compounds, the relatively high rates indicate that triplet excitons can be efficiently converted into singlet excitons through RISC, which has been well known as a key factor for OLED

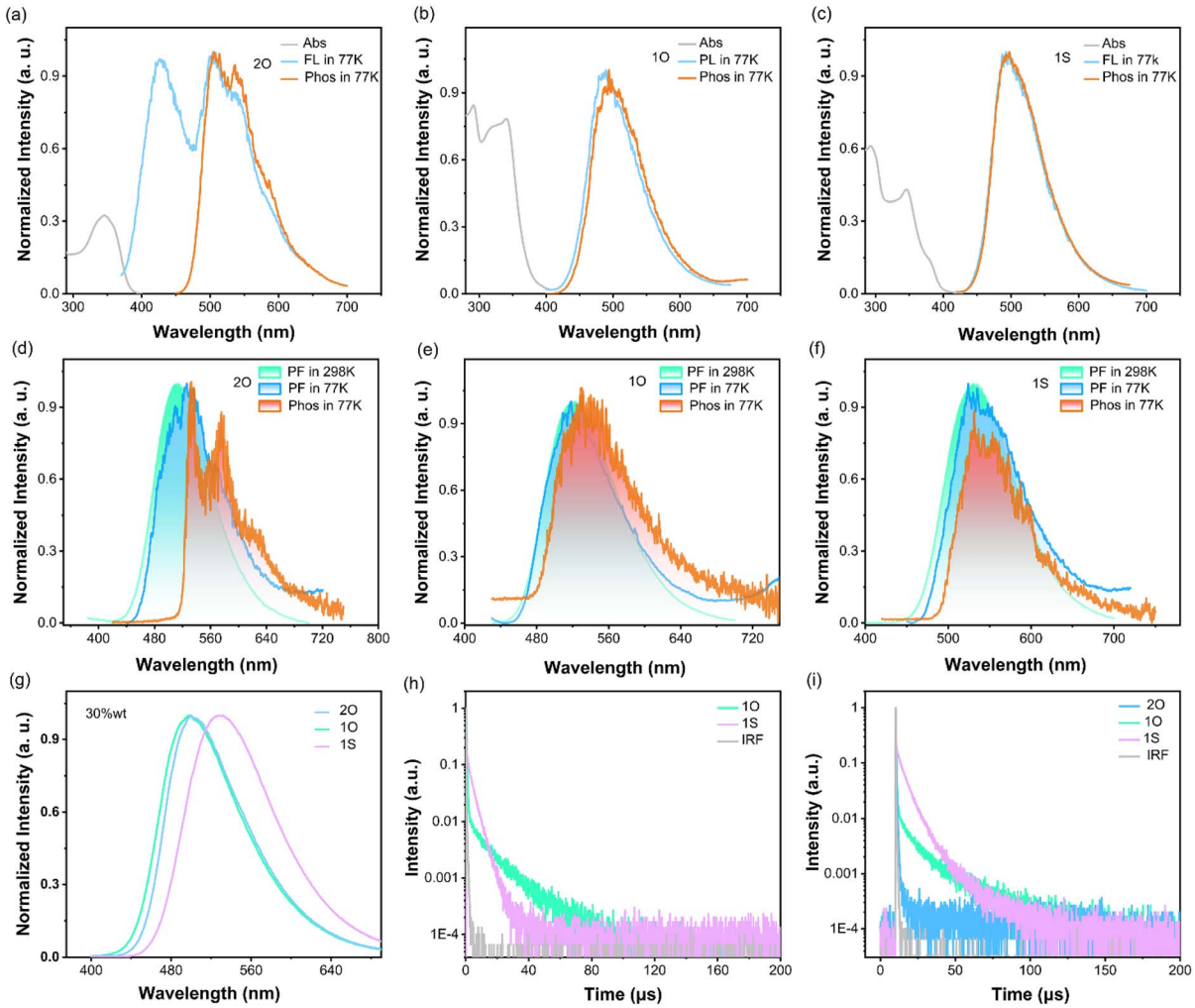

Fig. 2 Ultraviolet absorption (Abs) spectra, low-temperature fluorescence (FL) spectra, and low-temperature phosphorescence (Phos) spectra of **2O** (a), **1O** (b) and **1S** (c) in toluene solution; room- and low-temperature FL spectra and low-temperature Phos spectra of **2O** (d), **1O** (e) and **1S** (f) in neat films; room-temperature FL spectra of these three sensitizers in doped (g) films; transient PL decay curves in the neat (h) and doped (i) films at the microsecond scale. The excitation wavelength for the spectrum is 380 nm.

Table 1 Photophysical properties of **2O**, **1O**, and **1S** in neat and doped (30 wt% in TCTA) films

Film	Structure	λ_{em} (nm)	Φ_{PL}/Φ_d[a] (%)	τ_p (ns)	τ_d (μs)	ΔE_{ST} (eV)	$k_{r,S}$[b] (10^6 s^{-1})	$k_{nr,S}$[b] (10^6 s^{-1})	k_{ISC}[b] (10^6 s^{-1})	k_{RISC}[b] (10^5 s^{-1})
Neat	**2O**	511	9.7/-	63.6	—	0.37	1.53	14.2	—	—
	1O	520	39.3/17.9	162.8	14.23	0.11	1.31	2.03	2.74	1.29
	1S	531	20.4/15.7	76.8	3.56	0.09	0.61	2.38	9.09	12.1
Doped	**2O**	498	23.6/-	82.7	—	—	2.85	9.24	—	—
	1O	500	72.4/29.3	135.6	17.12	—	3.18	1.21	2.94	0.98
	1S	528	63.5/52.8	63.6	7.07	—	1.69	0.97	12.4	8.36

[a] Total/delayed PLQY values. [b] Calculated with the assumption of $k_{nr,T} = 0$ and $k_{r,T} = 0$.

applications. Therefore, **1O** and **1S** are likely good candidates for sensitizer applications in devices.

More factors may influence the photophysical dynamics of these molecules. The absolute photoluminescence quantum yields (PLQYs) of neat and doped thin films at 300 K are listed in Table 1. The PLQYs of **1O**, **1S**, and **2O** in neat thin films are 39.3%, 20.4%, and 9.7%, respectively, and increase to 72.4%, 63.5%, and 23.6% in doped thin films, respectively. The relatively low PLQYs in neat thin films may be due to strong intermolecular interactions, which can easily lead to π–π stacking or molecular aggregation and consequently enhance non-radiative energy transitions (exciton quenching) and self-quenching. By doping with an appropriate host material, the intermolecular distance in the film increased. Such a change can reduce direct

molecular interactions and suppress aggregation-caused quenching, thereby improving the emission efficiency.

At the cryogenic temperature of 77 K, the thermal broadening effect is significantly reduced, making any hidden anharmonic peaks more detectable. Note that even minimal anharmonicity would induce noticeable peak splitting. As shown in Fig. 2e and f, the low-temperature fluorescence spectra of **1O** and **1S** exhibit single peaks without characteristic Fermi resonance splitting, indicating an extremely small anharmonic coupling constant (V_3). This confirms that the vibrational behavior predominantly follows the harmonic oscillator model.

Photophysical processes in the presence of sensitizers

Apart from the TADF dynamics, we further studied the non-radiative transition processes of different systems in the presence of sensitizers on the basis of theoretical calculations of transition rate constants. We focused on the rates of intermolecular EnT processes as well as the ISC rates from singlet to triplet states. All EnT rates were obtained based on Fermi's golden rule and electronic structure calculations at the *ab initio* level. The ISC rates of **1O** and **1S** were extracted from Table 1, while those of **2O**, TCTA and the Ir(III) complex were computed based on the Marcus theory and electronic structure calculations at the *ab initio* level (see Table S10). Three types of systems were investigated: binary systems involving the host TCTA and a sensitizer molecule as the emitter, ternary systems that consist of the host TCTA, a sensitizer molecule and the Ir(III) complex emitter, and binary systems involving a sensitizer molecule as the host material compound and the Ir(III) complex emitter. The theoretical model diagram can be seen in Fig. 3.

The results of binary systems are summarized in Fig. 4. After the host TCTA absorbs photons and reaches the S_1 state, the excitons can undergo two pathways. One is the direct channel, in which a FRET process occurs to generate the S_1-state sensitizer. Another is the indirect channel, in which TCTA converts to its T_1 state *via* intersystem crossing at the beginning, followed by a TTET process to promote the sensitizer to its T_1 state and a possible reverse intersystem crossing to finally produce the S_1-state sensitizer. The transition rates of these processes might correlate with the PLQYs of **1O**, **1S**, and **2O** in doped thin films.

Under photoexcitation, the photophysical behaviors of the **2O**, **1O**, and **1S** binary systems exhibit some differences. For the **2O** binary system, the TTET channel is blocked by the large triplet-state conformational change of **2O** (RMSD = 0.60 Å), while the FRET rate related to the direct pathway is estimated to be 7.8×10^7 s^{-1}. For the **1O** and **1S** binary systems, the direct channels are preferred with the FRET rates at 1.9×10^6 and 4.8×10^8 s^{-1}, respectively. The RISC process dominates the efficiency of indirect channels and is one order of magnitude slower than FRET for **1O** and **1S**. On one hand, the relatively rapid FRET of the **1S** system may lead to its high PLQY. On the other hand, it was experimentally measured that the non-radiative decay rate of **2O** is stronger than its radiative decay rate (see Table 1), indicating a side channel in its direct pathway. Meanwhile, the alternative indirect pathway is accessible for **1O** and **1S** but obstructed for **2O**, agreeing well with their different PLQYs.

Analysis of the ternary systems can help us better understand the performance of electroluminescent devices such as EQE. Starting from TCTA (S_1), three possible pathways were proposed. First, the ISC transition may occur in the S_1 state of TCTA, followed by two successive TTET processes to produce the Ir(III) complex in its T_1 state *via* the triplet sensitizer (denoted as ISC–TTET–TTET). Second, the sensitizer can jump to the S_1 state *via* FRET from TCTA (S_1) and then switch to sensitizer (T_1), followed by TTET to generate the triplet Ir(III) complex (denoted as FRET–ISC–TTET). Third, the sensitizer exciton in its S_1 state possibly undergoes another FRET process and promotes the Ir(III) complex to its S_1 state, followed by the ISC to the T_1 state in the last step (denoted as FRET–FRET–ISC). Unlike photoexcitation for binary systems, the electroluminescent ternary systems can also start from TCTA (T_1), leading to

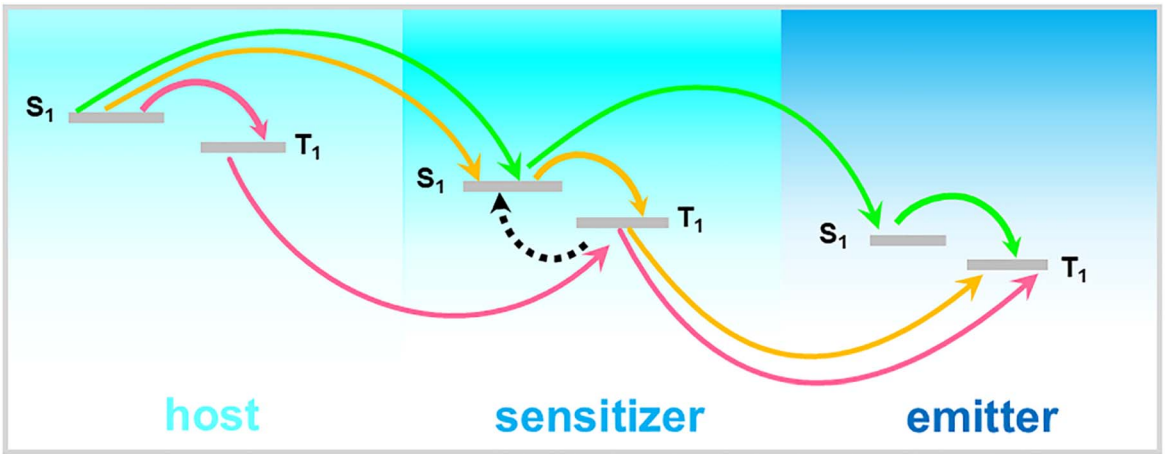

Fig. 3 The theoretical model diagram for sensitizers with host and emitter molecules. Different colors of arrows represent different pathways in ternary systems (ISC–TTET–TTET and TTET–TTET in red, FRET–ISC–TTET in yellow, FRET–FRET–ISC in green, and RISC in black), which can be simplified to represent pathways in binary systems.

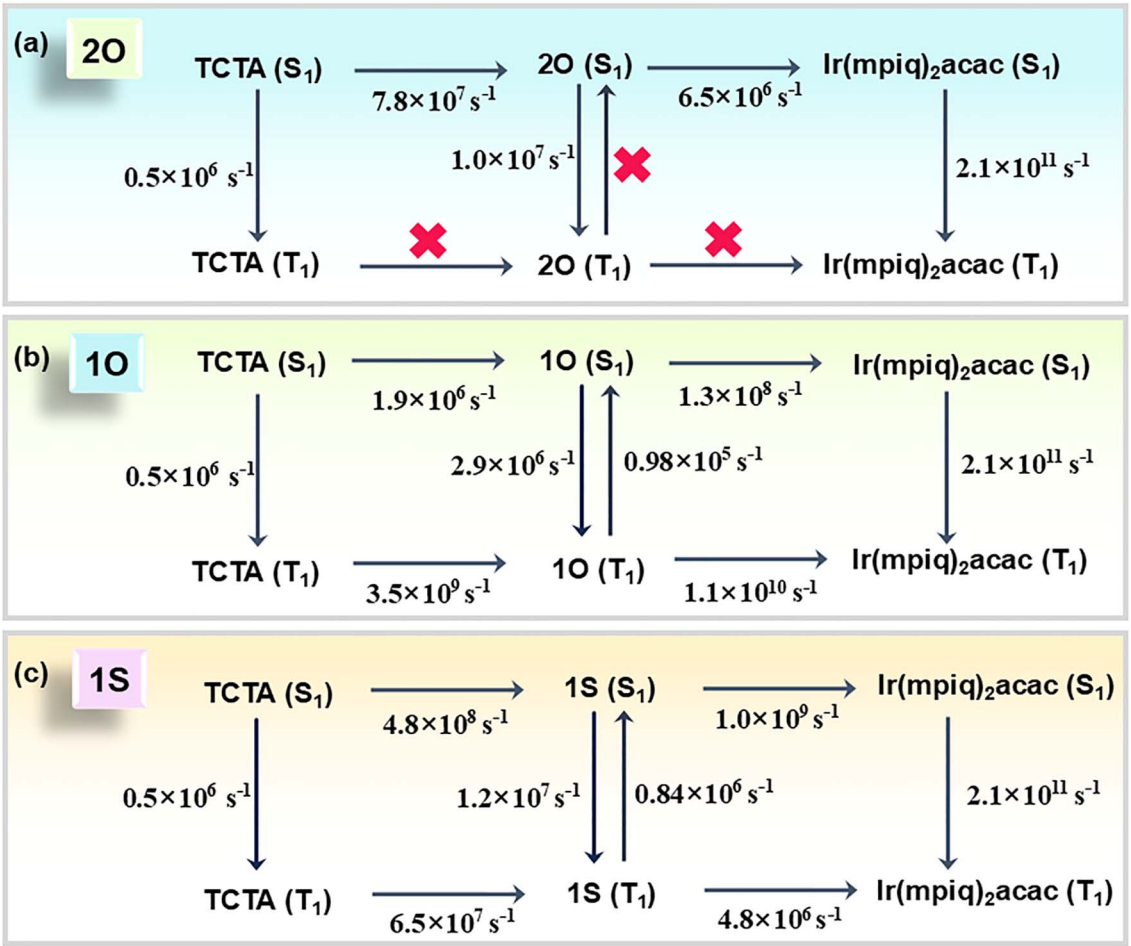

Fig. 4 Transition rates of photophysical processes in the presence of 2O (a), 1O (b), and 1S (c) as sensitizers.

the fourth pathway as TTET–TTET (*i.e.*, the first pathway without ISC for TCTA in the first step).

Different photophysical behaviors of the **2O**, **1O**, and **1S** as sensitizer in ternary systems are summarized in Fig. 4. Similar to the binary system, the key factor in the relaxation process of the **2O** ternary system is the severe conformational distortion between the T_1 and S_0 states of **2O**, which seriously impedes all pathways involving TTET. Only the FRET–FRET–ISC channel works with a modest efficiency determined by the energy transfer process from the **2O** sensitizer to the Ir(III) complex (6.5×10^6 s^{-1}). For the **1O** system, the T_1 excitons undergo effective TTET–TTET at the timescale of nanoseconds (3.5×10^9 s^{-1}), while the S_1 excitons possibly transfer to the triplet Ir(III) complex through ISC–TTET–TTET, FRET–ISC–TTET, or FRET–FRET–ISC. All three processes take place at the timescale of microseconds. The pattern of the **1S** ternary system is different from that of **1O**. On one hand, the transition rate of TTET–TTET starting from TCTA (T_1) is reduced to the timescale of microseconds (4.8×10^6 s^{-1}). On the other hand, the most rapid relaxation channel of the S_1 excitons is FRET–FRET–ISC with the rate-determining step as the FRET from the host TCTA to the **1S** sensitizer (4.8×10^8 s^{-1}). Additionally, its TADF characteristic might enhance the efficiency of reverse ISC from **1S** (T_1) to **1S** (S_1) and provide an auxiliary channel for the T_1 excitons.

Another type of binary system by excluding the wide-gap host TCTA from the corresponding ternary system may eliminate redundant energy transfer pathways and possibly achieve more efficient exciton management. Take the **1O** sensitizer as an example. In such a binary system, the energy transfer step from TCTA to **1O**, which is less efficient than that from **1O** to the Ir(III) complex, is removed, prompting the rates of TTET and FRET to 1.1×10^{10} and 1.3×10^8 s^{-1}, respectively. The same tendency can be observed on the FRET–FRET–ISC channel for the **1S** binary system, in which the EnT rate for the rate-determining step increases from 4.8×10^8 to 1.0×10^9 s^{-1}. All theoretical research results recommend **1O** and **1S** as excellent candidates for host or sensitizer materials in devices.

The efficiency of photophysical processes of different sensitizers can be affected by different factors. First, conformational mismatch between the singlet and triplet **2O** seriously suppresses the TTET channel, which should be responsible for its restricted performance in all systems. This suggests we pay more attention to molecular rigidity under excitation when we design a new sensitizer. Second, the multi-channel energy transfer capability of **1O** makes a strong contribution to enhancing exciton utilization. Finally, the TADF characteristic of **1S**, which further corresponds to heavy atoms and a small S_1–T_1 energy gap, provides an opportunity for T_1 excitons to utilize

the ultrafast FRET channel. It means that the strategy for designing a TADF emitter, for example, by introducing a multi-resonance structure or decreasing the intramolecular distance between donor and acceptor groups, can be directly applied to a sensitizer.

The relationship between the molecular structure and energy transfer efficiency can be understood based on Tables 2 and 3. First of all, as long as the sensitizer undergoes a large conformational change in different electronic states, the related energy transfer pathways would be completely obstructed. The structural rigidity becomes dominant in this case. The rates of TTET are also strongly influenced by electron exchange couplings (see Table 3). It would be very useful to carefully view the frontier molecular orbitals of the host-sensitizer and sensitizer-emitter complexes when we design a ternary OLED device. In contrast, the Franck–Condon term may play an important role in the efficiency of FRET. Except for molecular rigidity, the vibrational modes of sensitizers and anharmonic and Duschinsky effects should be studied with more sophisticated theoretical models in future research. Additionally, binary systems in which the sensitizer acts as a host are expected to exhibit superior efficiency in next-generation OLED devices relative to their ternary counterparts, owing to their simplified energy transfer pathways and accelerated charge transport kinetics.

Despite the similar molecular structures of sensitizers **1O** and **1S**, they exhibit distinct TTET rates (1.1×10^{10} s^{-1} for **1O** → Ir and 4.8×10^{6} s^{-1} for **1S** → Ir), which originate from the synergistic effects of Franck–Condon factors and electronic coupling integrals. The former can be seen in Fig. S18. During the $S_0 \rightarrow T_1$ transition of **1O**, the molecular configuration maintains good planarity (RMSD = 0.10 Å) with minimal C–O–C bond length changes (Δr < 0.02 Å). This structural rigidity results in high vibrational wavefunction overlap and a large FC factor (104.51 $hartree^{-1}$). In contrast, the steric repulsion between the sulfur atom's lone pairs and aromatic π–electrons in **1S** may lead to approximately 5–10° torsion on the C–S–C bridge, resulting in more significant geometric changes (RMSD = 0.21 Å and $\Delta r \sim 0.05$ Å) and a reduced FC factor (26.44 $hartree^{-1}$). The difference in the electronic couplings can be seen in Fig. S19. The smaller van der Waals radius of oxygen in the **1O**–Ir complex enables closer D–A stacking (4 Å), enhancing orbital overlap and electronic coupling (10^{-10} $hartree^2$). Conversely, the larger sulfur atom in the **1S**–Ir complex increases the intermolecular distance between the donor and acceptor (5.8 Å) and causes orientation deviation, finally weakening orbital overlap and electronic coupling (10^{-13} $hartree^2$). Except for the well-known heavy-atom effect during the O → S substitution in sensitizer design, our results suggest further optimizations on vibrational coupling in donor–acceptor complexes (*e.g.*, by selecting more rigid frameworks) and excited-state geometric displacement (*e.g.*, through intramolecular constraints to enhance complex rigidity).

In brief, theoretical research on photophysical processes of sensitizers reveals that an ideal sensitizer should simultaneously possess multi-path energy transfer capabilities in addition to conformational rigidity and TADF properties as exemplified by Monkman *et al.*[52] More importantly, careful design of binary and ternary sensitized systems is essentially required, such as enhancing intermolecular electronic coupling and minimizing intermediate losses. Besides the well-known TADF characteristics, an effective energy transfer process between the host, sensitizer, and emitter, either FRET or TTET,

Table 2 Adiabatic excitation energies of the donor and acceptor (E_d and E_a, kcal mol^{-1}), root mean square deviations between the optimized geometries of energy minima in ground and singlet excited states ($RMSD_d$ and $RMSD_a$, Å), Franck–Condon terms in eqn (2) (FC, $hartree^{-1}$), the square of electronic couplings in eqn (5) ($|H_{12}|^2$, $hartree^2$), and the calculated rates (k_{EnT}, s^{-1}) of the Förster resonance energy transfer processes

	E_d (kcal mol^{-1})	E_a (kcal mol^{-1})	$RMSD_d$ (Å)	$RMSD_a$ (Å)	FC term ($hartree^{-1}$)	$\lvert H_{12}\rvert^2$ ($hartree^2$)	k_{EnT} (s^{-1})
TCTA–**2O**	73.6	78.4	0.21	0.34	0.07	4.29×10^{-9}	7.8×10^{7}
TCTA–**1O**	73.6	70.3	0.21	0.42	0.07	1.12×10^{-10}	1.9×10^{6}
TCTA–**1S**	73.6	56.8	0.21	0.34	3.00	6.18×10^{-10}	4.8×10^{8}
2O–Ir	78.4	56.1	0.34	0.09	9.76	2.52×10^{-12}	6.5×10^{6}
1O–Ir	70.3	56.1	0.42	0.09	1.47	3.25×10^{-10}	1.3×10^{8}
1S–Ir	56.8	56.1	0.34	0.09	3.04	1.27×10^{-9}	1.0×10^{9}

Table 3 Adiabatic excitation energies of the donor and acceptor (E_d and E_a, kcal mol^{-1}), root mean square deviations between the optimized geometries of energy minima in ground and triplet excited states ($RMSD_d$ and $RMSD_a$, Å), Franck–Condon terms in eqn (2) (FC, $hartree^{-1}$), the square of electronic couplings in eqn (4) ($|H_{12}|^2$, $hartree^2$), and the calculated rates (k_{EnT}, s^{-1}) of the triplet–triplet energy transfer processes

	E_d (kcal mol^{-1})	E_a (kcal mol^{-1})	$RMSD_d$ (Å)	$RMSD_a$ (Å)	FC term ($hartree^{-1}$)	$\lvert H_{12}\rvert^2$ ($hartree^2$)	k_{EnT} (s^{-1})
TCTA–**2O**	73.3	61.6	0.20	0.60	—[a]	3.24×10^{-11}	—[a]
TCTA–**1O**	73.3	71.3	0.20	0.10	18.44	7.28×10^{-10}	3.5×10^{9}
TCTA–**1S**	73.3	55.5	0.20	0.21	24.36	1.02×10^{-11}	6.5×10^{7}
2O–Ir	61.6	51.6	0.60	0.09	—[a]	1.90×10^{-11}	—[a]
1O–Ir	71.3	51.6	0.10	0.09	104.51	4.04×10^{-10}	1.1×10^{10}
1S–Ir	55.5	51.6	0.21	0.09	26.44	6.96×10^{-13}	4.8×10^{6}

[a] The FC terms and EnT rates are neglected because of the large RMSD between **2O** (S_0) and **2O** (T_1).

also significantly contributes to achieving high EQE and low efficiency roll-off in OLED devices.

Electroluminescent devices

To validate the performance of **2O**, **1O**, and **1S** as the hosts and/or sensitizers in red phosphorescent devices, we constructed phosphorescent devices with the structure of ITO/HATCN (5 nm)/TAPC (40 nm)/TCTA (5 nm)/EML (20 nm)/B3PyMPM (0 or 5 nm)/DPPyA (55 or 50 nm)/LiF (0.8 nm)/Al (120 nm). Dihydropyrrolo[2,3-*f*:2′,3′-*h*]quinazoline-2,3,6,7,10,11-hexacyano (HATCN) and LiF were respectively employed as hole and electron injection layers; (1,1-bis[(di-4-methylphenyl)amine]phenyl)cyclohexane (TAPC) and (9,10-bis(6-phenylpyridin-3-yl)anthracene) (DPPyA) were used as hole and electron transporting layers; (4,6-bis(3,5-di(3-pyridyl) phenyl)-2-methylpyrimidine) (B3PyMPM) and TCTA served as hole and electron blocking layers. The emitting layer (EML) of ternary devices consisted of 65 wt% TCTA as the host material, 30 wt% **2O**, **1O**, or **1S** as the sensitizer and 5 wt% Ir(mpiq)$_2$acac as the terminal emitter. The EML of binary devices consists of 95 wt% **2O**, **1O**, or **1S** as the host material and 5 wt% Ir(mpiq)$_2$acac. Only the device with TCTA + Ir(mpiq)$_2$acac as the EML uses B3PyMPM as a hole blocking layer. The energy level diagram and chemical structures of the materials used in the device can be seen in Fig. S20 (see the SI). The external quantum efficiency–luminance (EQE–*L*) curves, electroluminescence spectra and current density–voltage–luminance (*J*–*V*–*L*) curves of the devices are displayed in Fig. 5a–c and S21 (see the SI), with the corresponding data summarized in Table 4.

Without adding any sensitizers, the device based on TCTA and Ir(mpiq)$_2$acac exhibited a low EQE$_{max}$ of 10.2%, a low maximum brightness (L_{max}) of 10 440 cd m^{-2} and a slightly high turn-on voltage (V_{on}) of 2.9 V (Fig. 5a and S21a). The device emitted red light with a peak wavelength at 640 nm, along with a weak band at around 450 nm (Fig. 5c and S22), which can be attributed to the emission of DPPyA. Such low EQE$_{max}$ may be due to the carrier imbalance and the loss of excitons in the ETL in the device. Therefore, when we added a 5 nm electron blocking layer and reduced the thickness of the electron transport layer by 5 nm, the EQE$_{max}$ increased notably to 22.7% along with a decrease of V_{on} (2.6 V) and an increase of L_{max} (13 700 cd m^{-2}) (Fig. 5a and S21a). However, there was still a significant efficiency roll-off of 32.2% at a brightness of 1000 cd m^{-2}.

When **2O**, **1O**, and **1S** were incorporated as sensitizers into the EML, the devices demonstrated higher EQE$_{max}$, smaller efficiency roll-off, higher L_{max}, lower V_{on} and pure red emission with a peak wavelength of around 637 nm, corresponding to

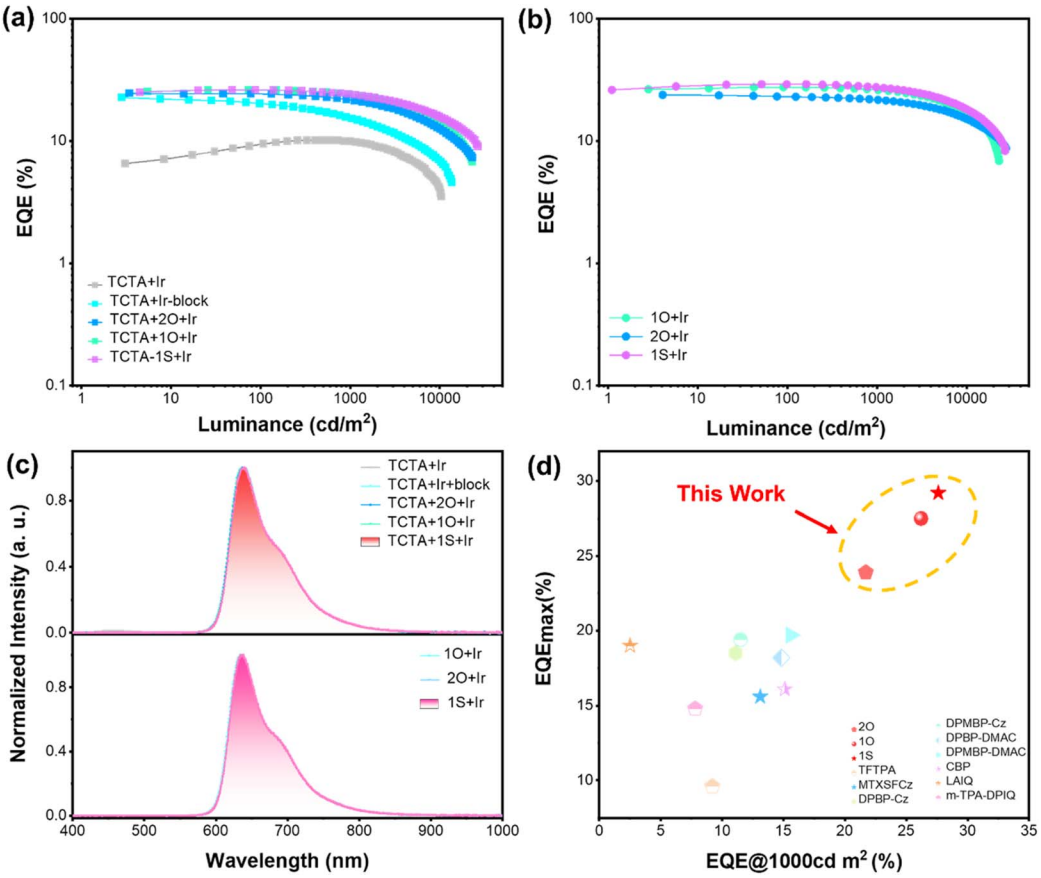

Fig. 5 External quantum efficiency *versus* luminance (EQE–*L*) curves for ternary (a) and binary (b) systems. (c) Normalized electroluminescence (EL) spectra of devices. (d) EQE comparison of OLED devices with binary EML structures based on Ir(mpiq)$_2$acac and its derivatives as phosphorescent emitters.

Table 4 Summary of performances of reference OLED devices based on TCTA and sensitized OLED devices based on **2O**, **1O**, and **1S**

	V_{on}[a] (V)	L_{max}[b] (cd m^{-2})	EQE_{max}[c] (%)	[d]EQE@1000 cd m^{-2} (%)	Roll off[e] (%)	λ_{EL}[f] (nm)	FWHM[g] (nm)	CIE(x, y)[h]
TCTA + Ir	2.9	10 440	10.2	9.9	2.9	640	63	(0.68, 0.29)
TCTA + Ir-block	2.6	13 700	22.7	15.4	32.2	640	63	(0.70, 0.30)
TCTA + **2O** + Ir	2.4	23 080	24.6	21.7	11.8	637	63	(0.70, 0.30)
TCTA + **1O** + Ir	2.5	22 940	26.2	24.0	8.4	637	60	(0.70, 0.30)
TCTA + **1S** + Ir	2.5	26 800	26.2	24.0	8.4	639	71	(0.70, 0.30)
2O + Ir	2.2	27 640	23.9	21.7	9.2	636	64	(0.70, 0.30)
1O + Ir	2.3	23 100	27.5	26.2	4.7	634	57	(0.70, 0.30)
1S + Ir	2.2	26 990	29.2	27.6	5.5	637	64	(0.70, 0.30)

[a] Turn-on voltage at 1 cd m^2. [b] Maximum brightness. [c] Maximum external quantum efficiency. [d] External quantum efficiency at a brightness of 1000 cd m^{-2}. [e] Efficiency roll off at a brightness of 1000 cd m^{-2} is calculated using (EQE_{max} − EQE@1000 cd m^{-2})/EQE_{max} × 100%. [f] Electroluminescence peak value. [g] Full width at half maximum. [h] Commission internationale de l'Eclairage color coordinates at a brightness of 1000 cd m^{-2}.

a CIE color coordinate of (0.70, 0.30), which means the complete energy transfer from TCTA and the sensitizer to the phosphorescent emitter. Specifically, the EQE_{max} and EQE@1000 cd m^{-2} significantly improved (Fig. 5a), reaching 24.6%/21.7%, 26.2%/24.0%, and 26.2%/24.0% for **2O**, **1O**, and **1S**, showing a significant lower efficiency roll-off of 11.8%, 8.4%, and 8.4%. Meanwhile, the L_{max} of the devices increased by 2–3 times, reaching 23 080 cd m^{-2}, 22 940 cd m^{-2}, and 26 800 cd m^{-2}, respectively, and V_{on} decreased below 2.6 V (Fig. S21a). Such outstanding device performances could be attributed to the following factors. Firstly, there are effective multi-channel energy transfer processes of sensitizers as mentioned above. For **1O** and **1S**, they have multi-channel energy transfer capabilities, enhanced intermolecular electronic couplings, and optimized vibrational modes and TADF properties, as shown in the above theoretical part, which are beneficial for energy transfer efficiency, whereas for **2O**, all triplet-state-involved channels are blocked by conformational mismatch, resulting in relatively limited performance. Secondly, these sensitizers possess bipolar charge transport properties with XT and TX groups for electron transport and a triphenylamine group for hole transport. Therefore, they play an important role in balancing the injection and transport of electrons and holes, reducing charge accumulation and exciton quenching, and thus alleviating efficiency roll-off at high current densities (Fig. 5a).

More importantly, theoretical calculations of energy transfer rates predict that binary systems by excluding the wide-gap host TCTA from the corresponding ternary system would eliminate redundant energy transfer pathways and achieve more efficient exciton management. Indeed, when we removed TCTA from the EML and used **2O**, **1O**, and **1S** as the host and sensitizer simultaneously, the EQE_{max} and EQE@1000 cd m^{-2} further improved for **1O** and **1S**, reaching 27.5%/26.2%, and 29.2%/27.6%, showing a much lower efficiency roll-off of 4.7% and 5.5% (Fig. 5b), which are consistent with theoretical calculations of energy transfer rates. However, for **2O**, the EQE_{max} was slightly decreased to 23.9%, which may be due to the inactive TADF properties of **2O** and inferior PLQY in the neat film (Table 1). Meanwhile, the V_{on} values of the devices based on **2O**, **1O**, and **1S** were all further lowered (Fig. S21(b)), showing better charge injection and transport. All the devices gave pure red emission with a CIE color coordinate of (0.70, 0.30), which means complete energy transfer from the sensitizer to the phosphorescent emitter (Fig. 5c). Notably, to the best of our knowledge, in OLED devices with a binary EML structure based on Ir(mpiq)$_2$acac and its derivatives as phosphorescent emitters, the **1S**-based binary device exhibited the highest EQE_{max} (29.2%) and EQE@1000 cd m^{-2} (27.6%) and high L_{max} (26 990 cd m^{-2}) (Fig. 5d, S23 and Table S11). Thus, theoretical calculations of energy transfer rates at the *ab initio* computational level provide structure–property relationships and rational guidance for OLED development. In future studies, theoretical-experimental collaborative explorations of more efficient sensitizers could achieve even higher performance in OLED devices.

Conclusions

In this work, we design three sensitizer molecules labelled as **2O**, **1O** and **1S** and systematically reveal their energy transfer mechanisms and performance optimization principles in OLED devices through a theoretical–experimental collaborative strategy. By modulating intramolecular distance between donor and acceptor groups (<5.5 Å), the designed molecules **1O** and **1S** achieve minimized singlet–triplet energy splitting (ΔE_{ST} < 3 kcal mol^{-1}) and suppressed structural distortion under excitation (RMSD < 0.34 Å), leading to excellent TADF properties. In contrast, **2O** exhibits compromised TADF characteristic because of its excessive ΔE_{ST} (17 kcal mol^{-1}) and severe structural mismatch (RMSD = 0.60 Å). We further implement theoretical calculations of energy transfer rates at the *ab initio* computational level. Specifically, for the ternary system that involves the host TCTA, a sensitizer molecule and the Ir(III) complex emitter, three possible pathways starting from the S_1 excitons are proposed as ISC–TTET–TTET, FRET–ISC–TTET, and FRET–FRET–ISC, along with a TTET–TTET channel starting from the T_1 excitons. Critical design principles for sensitizers are revealed based on the calculated transition rates of binary and ternary systems, including molecular rigidity under excitation, synergistic multi-channel energy transfer and intrinsic TADF properties. Multiscale structures of devices such as electronic

couplings between the host, sensitizer and emitter molecules should also be considered key factors in OLED development. Notably, the binary system involving the host **1S** and the Ir(III) complex emitter without the conventional host TCTA simplifies energy transfer pathways, thus achieving a high EQE_{max} of 29.2% with a negligible efficiency roll-off of 5.5% and an ultralow V_{on} of 2.2 V for red phosphorescent OLEDs, thereby surpassing ternary systems in overall performance. In brief, we propose the first theoretical model based on highly accurate calculations of excited-state electronic structures and non-radiative transition rates to represent dynamic behaviors of sensitizers in OLEDs and establish a cross-scale molecular-device co-optimization paradigm for next-generation high-efficiency OLED technologies. In future research, we will apply this theoretical model to blue/green-emitting systems and further develop multi-sensitizer synergy to achieve full-color high-performance electroluminescence.

Author contributions

Xiao Liu designed the experiments, synthesized the compounds, performed characterization, collected and analyzed the data, and conducted theoretical calculations. Xueliang Wen and Juan Qiao were responsible for device characterization, testing, and modifications. Xiao Liu, Lin Shen, and Xuebo Chen co-wrote and revised the manuscript. Wei-hai Fang provided computational guidance. Qian Wang, Lin Liu, Yibo Shi, Wei Sun, and Kai Feng participated in partial experimental data organization and verification. Yang Zhou and Chao Tang completed part of the calculations. Diandong Tang installed the software. Xuebo Chen supervised the project. All authors contributed to discussions and manuscript revisions.

Conflicts of interest

The authors declare no conflict of interest.

Data availability

CCDC 2443285–2443287 contain the supplementary crystallographic data for this paper.[56–58]

The data supporting this article have been included as part of the SI. General information, synthesis and characterization, X-ray crystallography, OLED fabrication and measurement, estimation of photophysical parameters, thermal and electrochemical properties, photoluminescence properties, supplemental theoretical calculations, OLED device data, NMR and HRMS, tables for the absolute and relative energies and Cartesian coordinates. See DOI: **https://doi.org/10.1039/d5sc03817k**.

Acknowledgements

We acknowledge the financial support from the National Key R&D Program of China (2022YFB3603001) and National Natural Science Foundation of China (22393914, W2441007, 22120102005, and 22193041).

Notes and references

1 W. Wang, Y. Zhou, L. Yang, X. Yang, Y. Yao, Y. Meng and B. Tang, *Adv. Funct. Mater.*, 2022, **32**, 2204744.
2 X. Ai, E. W. Evans, S. Dong, A. J. Gillett, H. Guo, Y. Chen, T. J. H. Hele, R. H. Friend and F. Li, *Nature*, 2018, **563**, 536–540.
3 M. Sudhakar, T. E. Djurovich and M. E. Thompson, *J. Am. Chem. Soc.*, 2003, **125**, 7796–7797.
4 M. Sudhakar, P. I. Djurovich and M. E. Hogen-Esch, *J. Am. Chem. Soc.*, 2003, **125**, 7796–7797.
5 T.-L. Wu, M.-J. Huang, C.-C. Lin, P.-Y. Huang, T.-Y. Chou, R.-W. Chen-Cheng, H.-W. Lin, R.-S. Li and C.-H. Cheng, *Nat. Photonics*, 2018, **12**, 235–240.
6 D. D. Zhang, L. Duan, C. Li, Y. L. Li, H. Y. Li, D. Q. Zhang and Y. Qiu, *Adv. Mater.*, 2014, **26**, 5050–5055.
7 M. A. Baldo, D. F. O'Brien, Y. You, A. Shoustikov, S. Sibley, M. E. Thompson and S. R. Forrest, *Nature*, 1998, **395**, 151–154.
8 X. Z. Song, D. D. Zhang, Y. Lu, C. Yin and L. Duan, *Adv. Mater.*, 2019, **31**, 1901923.
9 P. Heimel, A. Mondal, F. May, W. Kowalsky, C. Lennartz, D. Andrienko and R. Lovrincic, *Nat. Commun.*, 2018, **9**, 4990.
10 G. S. Lee, K. M. Hwang, I. Kang, S. H. Hong, S. Kim, Y. Jeong, R. Elumalai, S. B. Ko, T. Kim and Y. H. Kim, *Adv. Opt. Mater.*, 2025, **13**, 2402230.
11 A. Endo, M. Ogasawara, A. Takahashi, D. Yokoyama, Y. Kato and C. Adachi, *Adv. Mater.*, 2009, **21**, 4802–4806.
12 H. Uoyama, K. Goushi, K. Shizu, H. Nomura and C. Adachi, *Nature*, 2012, **492**, 234–238.
13 H. Kaji, H. Suzuki, T. Fukushima, K. Shizu, K. Suzuki, S. Kubo, T. Komino, H. Oiwa, F. Suzuki, A. Wakamiya, Y. Murata and C. Adachi, *Nat. Commun.*, 2015, **6**, 8476.
14 J. W. Sun, J. H. Lee, C. K. Moon, K. H. Kim, H. Shin and J. J. Kim, *Adv. Mater.*, 2014, **26**, 5684–5688.
15 X. Tang, L.-S. Cui, H.-C. Li, A. J. Gillett, F. Auras, Y.-K. Qu, C. Zhong, S. T. E. Jones, Z.-Q. Jiang, R. H. Friend and L.-S. Liao, *Nat. Mater.*, 2020, **19**, 1332–1338.
16 X.-Q. Wang, S.-Y. Yang, Q.-S. Tian, C. Zhong, Y.-K. Qu, Y.-J. Yu, Z.-Q. Jiang and L.-S. Liao, *Angew. Chem., Int. Ed.*, 2021, **60**, 5213–5219.
17 Y. Wada, H. Nakagawa, S. Matsumoto, Y. Wakisaka and H. Kaji, *Nat. Photonics*, 2020, **14**, 643–649.
18 K. Goushi, K. Yoshida, K. Sato and C. Adachi, *Nat. Photonics*, 2012, **6**, 253–258.
19 Y. Tao, K. Yuan, T. Chen, P. Xu, H. Li, R. Chen, C. Zheng, L. Zhang and W. Huang, *Adv. Mater.*, 2014, **26**, 7931–7958.
20 X. Xie, T. Gao, S. Shen, Z. Pang, Y. Qin, X. Lv and Y. Wang, *Org. Lett.*, 2024, **27**, 202–206.
21 C. Wang, L. Liu, W. Sun, J. J. Wang, Q.-K. Li, K. Feng, B. Liao, W.-H. Fang and X. B. Chen, *Adv. Opt. Mater.*, 2024, **13**, 2402317.
22 C. Adachi, M. A. Baldo, M. E. Thompson and S. R. Forrest, *J. Appl. Phys.*, 2001, **90**, 5048–5051.

23 Q. Wang, I. W. H. Oswald, X. Yang, G. Zhou, H. Jia, Q. Qiao, Y. Chen, J. Hoshikawa-Halbert and B. E. Gnade, *Adv. Mater.*, 2014, **26**, 8107–8113.
24 H. Tsujimoto, D.-G. Ha, G. Markopoulos, H. S. Chae, M. A. Baldo and T. M. Swager, *J. Am. Chem. Soc.*, 2017, **139**, 4894–4900.
25 N. M. Michielsen, S. M. Goodman, V. Soarimalala, A. A. E. van der Geer, L. M. Dávalos, G. I. Saville, N. Upham and L. Valente, *Nat. Commun.*, 2023, **14**, 14.
26 T. Förster, *Discuss. Faraday Soc.*, 1959, **27**, 7–17.
27 D. L. Dexter, *J. Chem. Phys.*, 1953, **21**, 836–850.
28 J. Lim, K. Y. Hwang, S.-Y. Kwak, S. M. Cho, J.-M. Kim and J. Y. Lee, *Adv. Opt. Mater.*, 2023, **11**, 2300672.
29 H. H. Cho, D. G. Congrave, A. J. Gillett, S. Montanaro, H. E. Francis, V. Riesgo-Gonzalez and H. Bronstein, *Nat. Mater.*, 2024, **23**, 519–526.
30 S. H. Lin, W. Z. Xiao and W. Dietz, *Phys. Rev. E*, 1993, **47**, 3698–3706.
31 H. Eyring, S. H. Lin and S. M. Lin, *Basic Chemical Kinetics*, Wiley, New York, 1980.
32 S. H. Lin, C. H. Chang, K. K. Liang, R. Chang, J. M. Zhang, T. S. Yang, M. Hayashi, Y. J. Shiu and F. C. Hsu, *Adv. Chem. Phys.*, 2002, **121**, 1–88.
33 S. H. Lin, *J. Chem. Phys.*, 1966, **44**, 3759–3767.
34 A. M. Mebel, M. Hayashi and S. H. Lin, *Chem. Phys. Lett.*, 1997, **274**, 281–292.
35 J. Han, L. Shen, X. B. Chen and W. H. Fang, *J. Mater. Chem. C*, 2013, **1**, 4227–4235.
36 J. Han, X. B. Chen, L. Shen, Y. Chen, W. H. Fang and H. B. Wang, *Chem.–Eur. J.*, 2011, **17**, 13971–13977.
37 L. S. Ma, W.-H. Fang, L. Shen and X. B. Chen, *ACS Catal.*, 2019, **9**, 3672–3684.
38 C. T. Lee, W. T. Yang and R. G. Parr, *Phys. Rev. B: Condens. Matter Mater. Phys.*, 1988, **37**, 785–789.
39 A. D. Becke, *J. Chem. Phys.*, 1993, **98**, 5648–5652.
40 T. Yanai, D. Tew and N. Handy, *Chem. Phys. Lett.*, 2004, **393**, 51–57.
41 D. Hegarty and M. A. Robb, *Mol. Phys.*, 1979, **38**, 1795–1812.
42 K. Andersson, P.-Å. Malmqvist and B. O. Roos, *J. Chem. Phys.*, 1992, **96**, 1218–1226.
43 P. Pulay, *Int. J. Quantum Chem.*, 2011, **111**, 3273–3279.
44 D. Roca-Sanjuán, F. Aquilante and R. Lindh, *J. Mol. Sci.*, 2012, **2**, 585–603.
45 G. Karlström, R. Lindh, P.-Å. Malmqvist, B. O. Roos, U. Ryde, V. Veryazov, P.-O. Widmark, M. Cossi, B. Schimmelpfennig, P. Neograd y and L. Seijo, *Comput. Mater. Sci.*, 2003, **28**, 222–239.
46 M. J. Frisch, G. W. Trucks, H. B. Schlegel, G. E. Scuseria, M. A. Robb, J. R. Cheeseman, G. Scalmani, V. Barone, G. A. Petersson, H. Nakatsuji *et al.*, *Gaussian 16, Revision A.03*, Gaussian, Inc., Wallingford, CT, 2016.
47 Y. T. Yang, L. Liu, W.-H. Fang, L. Shen and X. B. Chen, *JACS Au*, 2022, **2**, 2596–2606.
48 X. R. Zhang, L. Liu, W. J. Li, C. Wang, J. J. Wang, W.-H. Fang and X. B. Chen, *JACS Au*, 2023, **3**, 1452–1463.
49 P. A. M. Dirac, *Proc. R. Soc. London, Ser. A*, 1927, **114**, 243–265.
50 G. D. Scholes and K. P. Ghiggino, *J. Chem. Phys.*, 1994, **101**, 1251–1261.
51 Q. Y. Meng, H. Y. Shao, R. Wang, C. Y. Yao, Y. L. Wang, X. L. Wen, *et al.*, *Adv. Mater.*, 2024, **36**, 2407882.
52 K. Stavrou, L. G. Franca, A. Danos and A. P. Monkman, *Nat. Photonics*, 2024, **18**, 554–561.
53 H. Tsujimoto, D.-G. Ha, G. Markopoulos, H. S. Chae, M. A. Baldo and T. M. Swager, *J. Am. Chem. Soc.*, 2017, **139**, 4894–4900.
54 Y. Wada, H. Nakagawa, S. Matsumoto, Y. Wakisaka and H. Kaji, *Nat. Photonics*, 2020, **14**, 643–649.
55 X.-Q. Wang, S.-Y. Yang, Q.-S. Tian, C. Zhong, Y.-K. Qu, Y.-J. Yu, Z.-Q. Jiang and L.-S. Liao, *Angew. Chem., Int. Ed.*, 2021, **60**, 5213–5219.
56 X. Liu, X.-L. Wen, Y. Zhou, C. Tang, D. Tang, Q. Wang, Y. Shi, L. Liu, W. Sun, K. Feng, W.-H. Fang, J. Qiao, L. Shen and X. Chen, CCDC 2443285: Experimental Crystal Structure Determination, 2025, DOI: **10.5517/ccdc.csd.cc2n0fns**.
57 X. Liu, X.-L. Wen, Y. Zhou, C. Tang, D. Tang, Q. Wang, Y. Shi, L. Liu, W. Sun, K. Feng, W.-H. Fang, J. Qiao, L. Shen and X. Chen, CCDC 2443286: Experimental Crystal Structure Determination, 2025, DOI: **10.5517/ccdc.csd.cc2n0fpt**.
58 X. Liu, X.-L. Wen, Y. Zhou, C. Tang, D. Tang, Q. Wang, Y. Shi, L. Liu, W. Sun, K. Feng, W.-H. Fang, J. Qiao, L. Shen and X. Chen, CCDC 2443287: Experimental Crystal Structure Determination, 2025, DOI: **10.5517/ccdc.csd.cc2n0fqv**.